DYNAMICS OF THE PRIMARY CILIUM IN TIME-PERIODIC FLOWS

Y.-N. YOUNG

Abstract. In this work we investigate the dynamics of a non-motile primary cilium in time-periodic flows. The primary cilium is modeled as an elastic slender filament coupled to an elastic sheet with a local torque (mimicking the sub-axonemal anchorage) at the filament-sheet junction. We examine how a primary cilium responds to time-periodic flows depending on its axonemal stiffness and the initial base angle. In particular we focus on the tension and forces at the cilium base where ion channels are speculated to be "activated" by fluid flow via cilium bending. We find larger tension and forces at the ciliary base when the cilium is tilted. We further compare the cilium bending dynamics between oscillating and pulsing flows, and investigate the effect of oscillation frequency. From our simulation results we find that the cilium bending is not affected much by flow frequency, and different dynamics is found at different tilt angles.

1. Introduction

The primary cilium is a hair-like sensory organelle that protrudes from the apical cell membrane into the extra-cellular space. Figure 1 is an illustration of the cilium body connected to a basal body and the detailed sub-axonemal compartment. In differentiated non-mitotic cells of adult tissues and organs, the primary cilium is an isolated non-motile microtubule-based structure [3, 33]. The filamentary cilium body, also called axoneme, is made of nine microtubule doublets (see the cross section in figure 1) that are enclosed by the ciliary membrane which is a continuation of the cell's membrane. The axoneme is anchored and supported by the basal body that consists of the modified mother and daughter centrioles (microtubule organization centers, also known as MTOC). They are surrounded by distal and sub-distal appendages connecting to the cytoskeletal network. The anchorage below the basal body involves the basal feet that are associated with γ-tubulin, and unique filamentous structures known as striated rootlets [11]. Right above the basal body is a transition zone (TZ), where the Y-connectors bridge the microtubule doublets to the ciliary membrane (see figure 1). These Y-connectors distribute around the TZ microtubules in a more or less symmetrical fashion. The TZ is associated with various proteins and molecular motor transport. It is also found that the lipid composition and the permeability of the TZ membrane are slightly different than that of the ciliary membrane [17, 31].

Date: September 9, 2013.
1991 *Mathematics Subject Classification.* Primary 92C05, 76Z05; Secondary 74F10, 92B99.
Key words and phrases. Primary Cilium, Slender-Body Theory, Fluid-Structure Interaction.
The author was supported in part by NSF Grants CBET-0853673 and DMS-0708977.

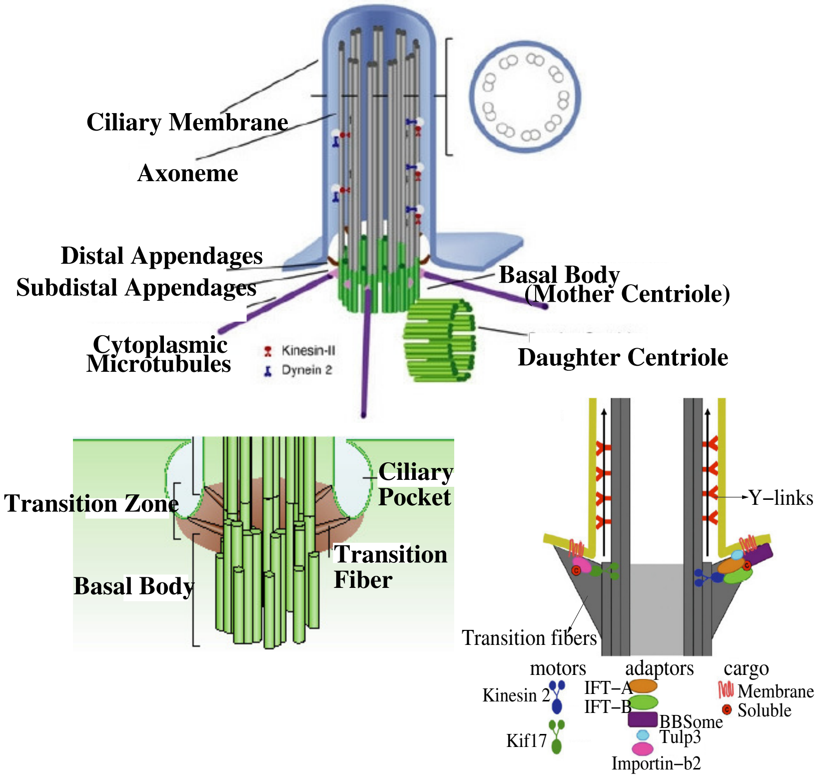

Figure 1. Top: Schematic diagram of primary cilium. Bottom: Sub-axonemal compartment (left from [17] and right from [8]).

Primary cilia are different from motile cilia in several important aspects: Primary cilia lack (a) a central pair of microtubule doublet, (b) connections between the outer doublets, and (c) other molecular machinery associated with motility. Unlike motile cilia, there is only one primary cilium per cell. Motile cilia are expressed on specialized cells while primary cilia are found on almost every cell type. Furthermore, primary cilia basal bodies have multiple basal feet and striated rootlets whereas motile cilia have only one of each [19].

In embryonic development primary cilia are known to rotate at certain frequencies and are involved in establishment of the left-right axis and anterior-posterior limb bud patterning [21, 12, 6] via sensing of the hedgehog and wnt families of morphogens. In non-mitotic differentiated cells of adult tissues and organs, primary cilia are non-motile, non-rotating, and only bend in response to the surrounding extracellular flow. For example, in the kidney cells, Praetorious and Spring found a dramatic extracellular calcium-dependent increase in intracellular calcium by bending primary cilia of the epithelial cells with fluid flow or micropipette manipulation. They also verified that this response was lost with removal of primary cilia [28, 29]. It has been suggested that this response occurs via polycystin-2, a cationic channel that localizes to the base of the cilium [1, 23]. This mechanism has also been found in liver cholangiocytes [22]. In addition to its role in flow-sensing, the primary cilium is involved in direct transmission of strains in cartilage extra cellular matrix.

Mechanosensory function of primary cilia has been suggested in other cell types as well, such as bone cells, human airway smooth muscle and epithelial cells.

Compared to motile cilia, a lot less theoretical modeling work on primary cilia can be found in the literature: Schwartz *et al.* [35] developed a mathematical model based on a small-deformation elastic beam formulation. They assumed a constant velocity and drag profile along the cilium, which was found to break down under high flow conditions. Resnick *et al.* [30] applied a similar formulation to study small deflections of the primary cilium in a cylindrical Poiseuille flow. Liu *et al.* [20] used a more refined model of the viscous flow around an array of cilia by numerically solving Stokes equations. They assumed small rotation at the cilium base and they compute the drag on cilium axoneme consistently from the Stokes equations. Rydholm *et al.* [32] conducted direct numerical simulations of the bending of an elastic filament connected to an elastic membrane. From their computations they found the stress distribution along a filament bent under flow with the maximum stress at the axoneme base. Unfortunately they did not provide any quantitative comparison of cilium bending under flow between simulations and experiments. Downs *et al.* [5] refined previous models [35, 20] by taking into account the large rotation at the cilium base and the consistent hydrodynamic drag force. They also used COMSOL CFD software to refine the viscous drag along a deflected elastic filament. Their results illustrate the importance of the interaction between fluid flow and the primary cilium axoneme for predicting the equilibrium profiles of primary cilia under flow

Recently Young *et al.* [40] conducted a quantitative comparison of cilium bending under a viscous flow using the slender-body theory (SBT), where the ciliary axoneme is modeled as an elastic slender filament in a steady Stokes flow. By comparing the equilibrium profiles of primary cilia under flow between experiment and modeling, the support from the basal body is found to behave like a nonlinear spring. They incorporated the nonlinear spring for the basal support into their slender-body modeling, and found good quantitative agreement in the bending dynamics of a primary cilium under flow between experiment and modeling. They further showed that nonlinear basal anchorage can be modeled as an elastic shell with a local torque at the junction with the axoneme [40].

The flow-induced bending of the primary cilia has been identified as an important biophysical signal in mechanotransduction. In *in vivo* situations, the primary cilia are often exposed to non-steady fluid flow. For example, bone tissue is immersed in a dynamic (and oscillatory) fluid flow driven by the arterial pressure head. In particular, it has been shown that different temporal dynamics of the fluid flows lead to different degree of stimulations [18, 4]. Pulsatile flow at low frequencies is found to be more effective (than steady flow and oscillating flow) in terms of stimulating the highest population of cells to trigger the subsequent signaling [18]. It is not clear if this finding is due to the mechanics of bending, structural response of the axoneme, or how the ion channels respond to stimuli at different frequencies. In this work we conduct a numerical study of the mechanics of cilium bending under both oscillating and pulsatile time-periodic flows. We focus on the mechanical responses of the axoneme to the dynamic flow with different axonemal bending stiffness, base angle and temporal variation of the flow (pulsing versus oscillating).

This paper is organized as follows. We formulate the elastic filament-sheet model in § 2. Based on the SBT we describe how an elastic filament can be supported by a local torque at the point where it connects with an elastic sheet. This model has been successfully applied to understand the dynamics of a bending cilium under a steady flow [40]. In § 3 we report numerical findings of the cilium bending dynamics under different conditions. In § 4 we provide a short summary and discussion on the future direction.

2. FORMULATION

For a primary cilium of length $L = 1$ μm bending by a uniform fluid flow of speed 1 cm$/s$, the ratio of inertial to viscous forces (Reynolds number) is of the order of 10^{-4} under typical physiological conditions. Hence in our formulation we ignore the inertia effects and consider the Stokes flow regime for the interaction between the primary cilium and the viscous fluid flow. The aspect ratio $\epsilon = r/L$ of a primary cilium is often in the range $10^{-2} \leq \epsilon \leq 10^{-1}$, with r the axonemal radius as shown in figure 2. Consequently the relevant physics is the bending of an anchored elastic slender filament in Stokesian flows. In the following formulation we simplify the coupling between the ciliary axoneme, plasma membrane and cytoskeleton network and focus on an elastic filament coupled to an elastic sheet (transition zone in figure 1 or region II in figure 2).

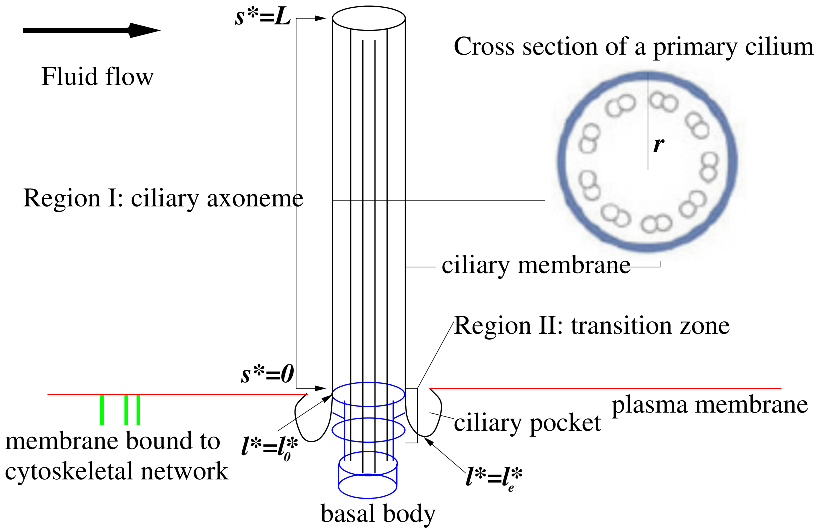

FIGURE 2. Illustration of the main features in the problem formulation. The axoneme is an elastic filament of length L and radius r (s^{*} is the dimensional arc length), and it is coupled to the transition zone (modeled as an elastic sheet), along which l^{*} is the dimensional arc length.

We adopt the elastic filament (or beam) formulation [10, 9, 26, 27] to model the bending of ciliary axoneme under fluid flow, and use the hydrodynamic load from the local drag model [37, 38, 39]. We denote the force distribution along the cilium as $\mathbf{F} = F^{t}(s)\hat{t} + F^{n}(s)\hat{n}$ with $s \in [0, 1]$ the arclength, and $\hat{t}$ and $\hat{n}$ the unit tangent and normal vectors, respectively. The curvature κ is assumed to be linearly proportional to the moment M: $M = E_{B}\kappa$ where E_{B} is the bending rigidity of the axoneme. The external load $\mathbf{P}(s) = P^{t}\hat{t} + P^{n}\hat{n}$ is related to the force by $\frac{d\mathbf{F}}{ds} + \mathbf{P} = \mathbf{F}_s + \mathbf{P} = 0$. The moment and the force density is related as $\frac{dM}{ds} = M_s = F^n$. Denoting the filament centerline $\mathbf{x} = (x(s), y(s))$ and the unit tangent vector $\hat{t} = (t_1(s), t_2(s))$, the governing equations are

$$x_s = t_1, \;\; y_s = t_2, \tag{2.1}$$

$$t_{1s} = -\kappa t_2, \;\; t_{2s} = \kappa t_1, \tag{2.2}$$

$$F_s^t = -\kappa F^n - P^t, \tag{2.3}$$

$$F_s^n = \kappa F^t - P^n, \tag{2.4}$$

$$\kappa_s = \frac{F^n}{E_B}. \tag{2.5}$$

The local filament inextensibility ($t_1 t_{1s} + t_2 t_{2s} = 0$) is utilized in deriving equations 2.2-2.4. The dimensionless tangential force and the tension force σ are related as $\sigma = F^t + \kappa^2$. The external load $\mathbf{P}$ is computed from the local SBT as

$$\mathbf{P} = -\frac{\eta\left(\partial \mathbf{x}/\partial t - U\right)}{\left(1+2\beta\right)\mathbf{I} + \left(1-2\beta\right)\mathbf{x}_s \otimes \mathbf{x}_s}, \tag{2.6}$$

where U is the fluid velocity at the location $\mathbf{x}$ in the absence of the elastic filament. $\beta = 1/(-\ln(\epsilon^2 e))$ is the filament slenderness and $\eta = \frac{8\pi\mu\dot{\gamma}L^4\beta}{E_B}$ is the effective viscosity [37, 38, 39] with μ the fluid viscosity and $\dot{\gamma}$ the characteristic flow rate. η is a ratio of viscous force to the bending force, and large η implies a more flexible filament under a given viscous stress.

The time-dependent filament dynamics is approximated by first discretizing the time derivative in equation 2.6 as

$$\frac{\partial \mathbf{x}}{\partial t} = \frac{1}{2\Delta t}\left(3\mathbf{x}^{k+1} - 4\mathbf{x}^{k} + \mathbf{x}^{k-1}\right) + O(\Delta t^3), \tag{2.7}$$

and the equations for the force distribution at the $k+1$st step are

$$\mathbf{F}_s^{k+1} + \mathbf{P}^{k+1} = \mathbf{F}_s^{k+1} - \frac{\eta\left(\frac{3\mathbf{x}^{k+1} - 4\mathbf{x}^{k} + \mathbf{x}^{k-1}}{2\Delta t} - U(\mathbf{x}^{k+1})\right)}{\left(1+2\beta\right)\mathbf{I} + \left(1-2\beta\right)\mathbf{x}_s^{k+1} \otimes \mathbf{x}_s^{k+1}} = 0. \tag{2.8}$$

At the $k+1$st time level we solve the following system of boundary-value equations

$$x_s^{k+1} = t_1^{k+1}, \;\; y_s^{k+1} = t_2^{k+1}, \tag{2.9}$$

$$t_{1s}^{k+1} = -\kappa^{k+1} t_2^{k+1}, \;\; t_{2s}^{k+1} = \kappa^{k+1} t_1^{k+1}, \tag{2.10}$$

$$\kappa_s^{k+1} = \frac{F^{n,k+1}}{E_B}, \tag{2.11}$$

together with the appropriate boundary conditions: At the free filament end ($s = 1$), the force-free and torque-free conditions give

$$F^t\left(1\right) = 0, \quad F^n\left(1\right) = 0, \quad \kappa\left(1\right) = 0. \tag{2.12}$$

At the filament basal body ($s = 0$) $x(0) = 0$ and $y(0) = 0$.

For a clamped filament the base angle θ_0 (with respect to the shear flow direction) is specified, while for a hinged filament the curvature at the base $\kappa(s = 0)$ is specified. From experiments we know that it is neither for a primary cilium under physiological conditions. In fact our previous work shows that there is a rotational stiffness, and the rotational stiffness (originated from the basal anchorage) behaves like a nonlinear rotational spring that can be explained by coupling the axoneme to an elastic sheet [40]. Assuming axial-symmetry for the elastic sheet, we parametrize

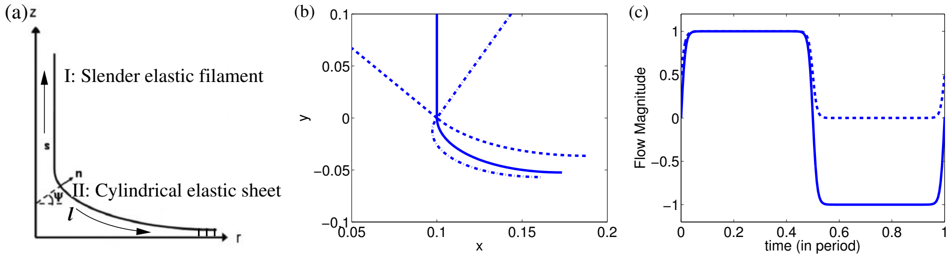

FIGURE 3. Panel (a): Coordinate system for the cylindrical elastic sheet in the transition zone. Region I is the slender filament, and region II is the cylindrical sheet where $\psi = \pi/2$ at the far end is fixed. Panel (b): Profiles of the filament-sheet system in a quiescent flow ($\eta = 0$) with different values for the torque h at the base. Panel (c): Flow magnitude for oscillating (solid) and pulsing (dashed) flows.

the sheet surface as $(r(l), z(l))$ with $l \in [l_0, l_e]$ the arc-length along the elastic sheet. ψ is the angle between the elastic shell normal vector $\mathbf{n}$ and the r-axis, see figure 3(a). The governing equations for the cylindrically symmetric, inextensible elastic sheet are [25, 34]

$$\frac{dr}{dl} = \sin\psi, \quad \frac{dz}{dl} = -\cos\psi, \tag{2.13}$$

$$\frac{d\psi}{dl} = -\nu + \frac{\cos\psi}{r}, \quad \frac{d\nu}{dl} = Q, \tag{2.14}$$

$$\frac{dT_m}{dl} = (T_\phi - T_m)\frac{\sin\psi}{r} - \kappa_m Q, \tag{2.15}$$

$$\frac{dQ}{dl} = T_m\kappa_m + T_\phi\kappa_\phi - \frac{\sin\psi}{r}Q, \tag{2.16}$$

with ν the moment of the cylindrical sheet, $\kappa_m = -\frac{d\psi}{dl}$, $\kappa_\phi = \frac{\cos\psi}{r}$, and $T_\phi = T_m + E_T\left(\kappa_m^2 - \kappa_\phi^2\right)$. E_T is the bending rigidity of the elastic sheet, and in the following we assume that the ratio of the two rigidities $\lambda \equiv E_T/E_B < 1$. At $l = l_0$ the elastic sheet is connected to the filament, and at $l = l_e$ it is connected to the surrounding membrane.

Equations 2.13-2.16 are coupled to equations 2.1-2.5 by the boundary conditions at the junction where the filament base ($s = 0$) is connected to the sheet ($l = l_0$). Firstly, the unit tangent vector is continuous: The filament tangent vector at the base is related to the angle ψ as

$$t_1(0) = -\sin\psi(l_0), \quad t_2(0) = \cos\psi(l_0).$$

Secondly, the force distribution and the curvature are also continuous at the junction

$$T_m(l_0) = F_t(0)\left(\frac{L_S}{L_B}\right)^2, \quad Q(l_0) = F_n(0)\left(\frac{L_S}{L_B}\right)^2,$$

where L_S and L_B are the characteristic lengths for the sheet and filament, respectively.

As explained in the introduction, the TZ fibers connect the TZ microtubules to the membrane. Here we assume that the mechanical support from the basal body can be modeled as a localized finite torque (from the transition fibers) on the elastic sheet at $l = l_0$. The equation for the moment along the ciliary axoneme is then

$$\frac{dM}{ds} = F^n(s) + h\delta\left(s\right), \tag{2.17}$$

where h is the magnitude of the torque at the base, and $\delta\left(s\right)$ is the Kronecker-delta function at $s = 0$. Integrating over a small interval around $s = 0$, we find that the localized torque (from the TZ fibers) induces a jump in the moment

$$M\left(0^+\right) = M\left(0^-\right) + h \to \kappa\left(0^+\right) = \kappa\left(0^-\right) + \frac{h}{E_B} = \frac{h}{E_B}, \tag{2.18}$$

which in turn induces a curvature at the cilium base because we assume linear elasticity for the axoneme.

At the junction the radius of the elastic sheet $r(l_0)$ is assumed to be equal to the axonemal radius r, and the height of the transition membrane $z(l_0) \sim r(l_0)$. At the opposite end point, the elastic sheet is assumed to be connected to the cell membrane in a flat angle such that $\psi(l_e) = \pi/2$. Equations 2.13-2.16 are rendered dimensionless by scaling the length to the filament radius r_f and force to E_B/r_f^2. Table I lists the relevant physical and dimensionless parameters in the model.

Table 1. Table I: List of physical and dimensionless parameters

E_B	bending rigidity of the ciliary axoneme	$\approx 8.4 \times 10^{-23} Nm^2$ from [40]
E_T	bending rigidity of the cylindrical sheet	$E_T = \lambda E_B$ with $\lambda < 1$
r	axonemal radius	$\approx 100nm$
L	axonemal contour length	$1\mu m \leq L < 15\mu m$
θ_0	cilium tilt angle	see discussion below
η	effective viscosity (ratio of viscous to elastic forces)	$0.1 \leq \eta < 10^2$ from [40]
ϵ	filament aspect ratio	$10^{-3} < \epsilon \leq 10^{-1}$
β	filament slenderness	$0.1 \leq \beta \leq 0.3$
h	local torque at the transition region	see discussion below

We solve the coupled boundary-value differential equations using the bvp4c solver in MATLAB. Figure 3(b) illustrates the cilium-transition zone profiles for different values of h. In the absence of viscous load (from fluid flow), a non-zero torque is needed to support the axoneme in the upright position because the unforced equilibrium is a flat horizontal shell connected to a horizontal straight filament. As the cilium basal body is mechanically connected to the ciliary membrane through the connectors and micro-tubular distal appendages, it is physiologically feasible that non-zero h corresponds to the support from the transitional fibers and other sub-axonemal anchorage that are connected to the ciliary membrane. Numerically we find that the value of h required to support the upright cilium axoneme is proportional to λ, and in dimensionless units $h = -0.145$ when $\lambda = 1/10$ and $h = -0.402$ when $\lambda = 1/3.6$. The tilt angle θ_0 is found to vary in experimental observations, and three representative values of θ_0 from [40] are used in the calculations.

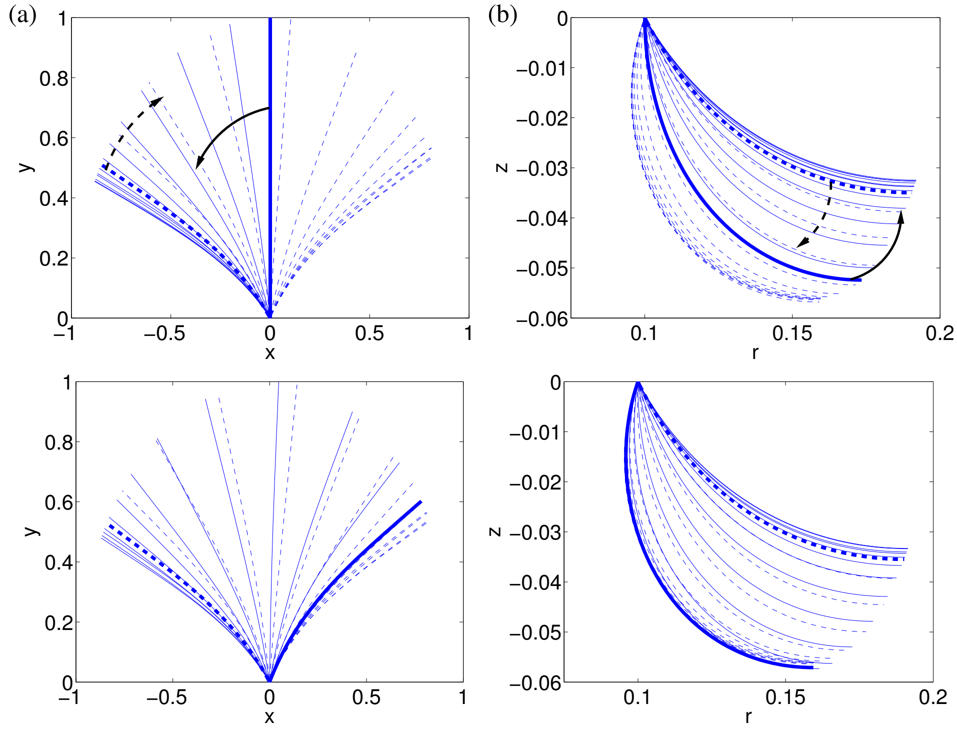

Figure 4. Top row: First period of oscillation of an elastic filament with $\eta = 20$ in an oscillating flow with periodicity $T = 10$. Bottom row: Second period from $t = 10$ to $t = 20$. Panel (a): Solid lines are from $t = 0$ (thick solid line) to $t = 5$ toward the left (solid arrow), with an interval of $\triangle t = 0.4$ between two adjacent solid lines. Dashed lines are from $t = 5.4$ (thick dashed line) to $t = 10$ toward the right (dashed arrow). Panel (b): Corresponding deformation of the elastic shell.

3. RESULTS

We apply the coupled model to examine the dynamics of a primary cilium under a periodic flow with either an oscillating magnitude (between −1 and 1) or a pulsing magnitude (between 0 and 1, see figure 3(c)). Such periodic flows are motivated by the physiological conditions in kidney and bone marrow, where primary cilia go through repetitive bending under a periodic fluid flow (see references in [18, 4]). It has also been observed that the basal anchorage may deteriorate due to repeated bending over a long time [18, 4]. This observation illustrates the complex nature of the support from the basal body and the surrounding cytoskeletal structures. Additional motivation is from a recent study where an oscillatory flow chamber is used to investigate how the cytoskeletal network responds to the mechanical load transferred from the ciliary axoneme to the basal body when primary cilia are exposed to a periodic hydrodynamic load [7].

For the following results the time-periodic flow is a 2D planar shear flow: $U = -A(t)(y, 0)$. The flow magnitude $A(t) = \tanh(10 \sin(\frac{2\pi t}{T}))$ for an oscillating flow and $A(t) = (1+\tanh(10\sin(\frac{2\pi t}{T})))/2$ for a pulsing flow. For all the results presented in this section the periodicity is fixed as $T = 10$. The ratio between the two bending rigidities is fixed as $\lambda = 0.2778$, and we adjust the torque h to change the base angle θ_0 at $t = 0$.

First in § 3.1 we focus on the dynamics of an upright primary cilium ($\theta_0(t = 0) = 0.5\pi$) with three different values of effective viscosity η. For a fixed fluid viscosity and flow rate, the effective viscosity η is small for a stiff axoneme while large η means the axoneme is flexible. In § 3.2-3.3 we study dynamics of filament bending at different initial tilt θ_0, which is determined by the balance of moments at the connection between the filament and the sheet in our model. By adjusting the torque h with everything else fixed, the cilium orientation varies from upright to tilted, as shown in figure 3(b). Finally we compare the bending dynamics between oscillating and the pulsing planar shear flow in § 3.4.

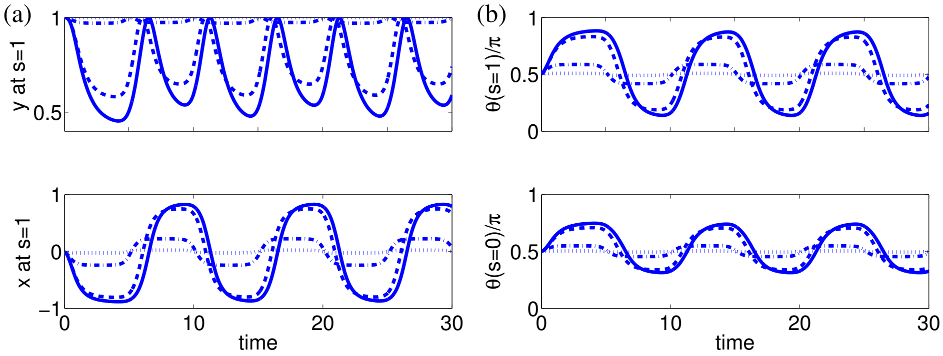

FIGURE 5. Panel (a): Location of the free end ($s = 1$). Panel (b): Angles at the free end (top) and the fixed end (bottom). $\eta = 0.1$ for the dotted lines, $\eta = 1$ for the dash-dotted lines, $\eta = 10$ for the long dashed lines, and $\eta = 20$ for the solid lines.

3.1. Upright position: $\theta_0(t = 0) = 0.5\pi$ in an oscillating flow.

The top row of figure 4 shows the dynamics of the filament (panel (a)) and the sheet (panel (b)) in the first period $0 \le t \le 10$. In both panels the thick solid lines are the initial profiles at $t = 0$. The solid lines are the profiles during the top half of the cycle, and the dashed lines are for the bottom half of the cycle. The time interval between two adjacent solid or two dashed curves is $\triangle t = 0.4$. As time progresses from 0 to $t = 5$ (solid arrows), the filament bends toward the left and reaches the equilibrium right before the flow changes direction at $t = 5$, when the filament begins to bend toward the right from the thick dashed lines (dashed arrows). In the simulations the filament-sheet takes on a periodic response to the flow after the first period. This periodic response is shown in the second row of figure 4, where the solid lines start from the thick solid line, complete the top half of the cycle, and then the dashed line start from the thick dashed line to complete the bottom half.

Figure 5 (a) shows the position of the filament free end as a function of time for four values of η. The corresponding angle at the free end and fixed end are shown in figure 5(b). For small η (stiff filament) the filament moves very little around the initial position, and the rigid filament rotates in sync with the oscillating

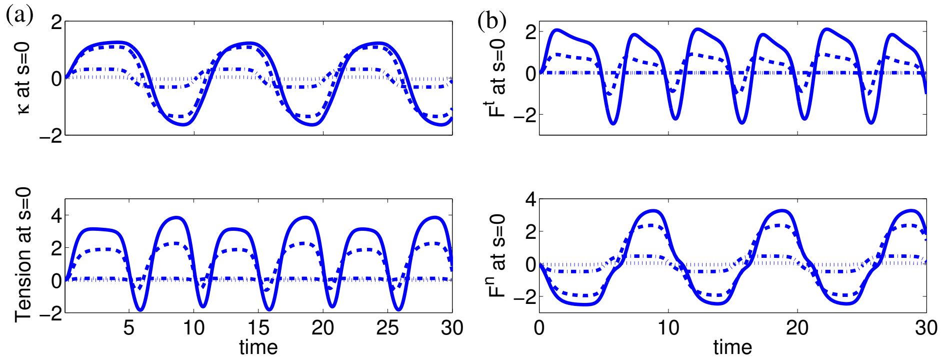

FIGURE 6. Panel (a): Curvature κ (top) and tension (bottom) at the fixed end. Panel (b): Tangential force F^t (top) and normal force F^n (bottom). $\eta = 0.1$ for the dotted lines, $\eta = 1$ for the dash-dotted lines, $\eta = 10$ for the long dashed lines, and $\eta = 20$ for the solid lines.

flow. For large η (flexible filament) both the filament deformation and rotation are large, and the response to the oscillating flow is not in sync. Figure 6(a) shows the corresponding variation of filament curvature (top panel) and filament tension (bottom panel) at the fixed end. Figure 6(b) shows the corresponding tangent force F^t (top) and normal force F^n (bottom) at the fixed end.

3.2. **Tilted position:** $\theta_0(t = 0) = 0.37\pi$ **in an oscillating flow.** We repeat the calculations for a filament with $\theta_0(t = 0) = 0.37\pi$ (thick solid line in figure 7(a)). The first period of oscillation is shown in the first row of figure 7: At $t = 0$ the cilium profile is the tilted thick solid curve, and it bends toward the left (solid arrow) in the first half of the cycle ($0 \le t \le 5$). For $5 \le t \le 10$ the filament bends from the thick dashed line toward the right (dashed arrow). Solid lines in panel (a) start from $t = 0$ (thick solid line) to $t = 5$ moving toward the left following the solid arrow, with an interval of $\triangle t = 0.4$ between two solid lines. Dashed lines start from $t = 5.4$ (thick dashed line) to $t = 10$ moving toward the right following the dashed arrow, with an interval of $\triangle t = 0.4$ between two dashed lines. The corresponding deformation of the elastic shell is shown in panel (b). During the first cycle from $t = 0$ to $t = 10$, the maximum cilium bending is reached before the reversal of flow. After the first cycle the cilium bending is periodic between the rightward and leftward cycles, and the second period is shown in the second row of figure 7. We see that the bending dynamics is asymmetric between leftward and rightward flow due to the tilt at filament base.

Figure 8 illustrate the dynamics of the filament free end position (left panels) and angle (right panels) for four values of η. For the stiff axoneme with $\eta = 0.1$, the response to the oscillatory flow is a more-or-less symmetric rotation around the initial profile. For the flexible axoneme with $\eta = 20$, the rotation at the base is very asymmetric, with the filament spending more time to the left of the initial profile. In addition the more flexible axoneme also lags behind the stiff axoneme in their response to the oscillatory flow. Figure 9 shows the corresponding curvature, tension, tangent force and normal force at the fixed end. The curvature and tension

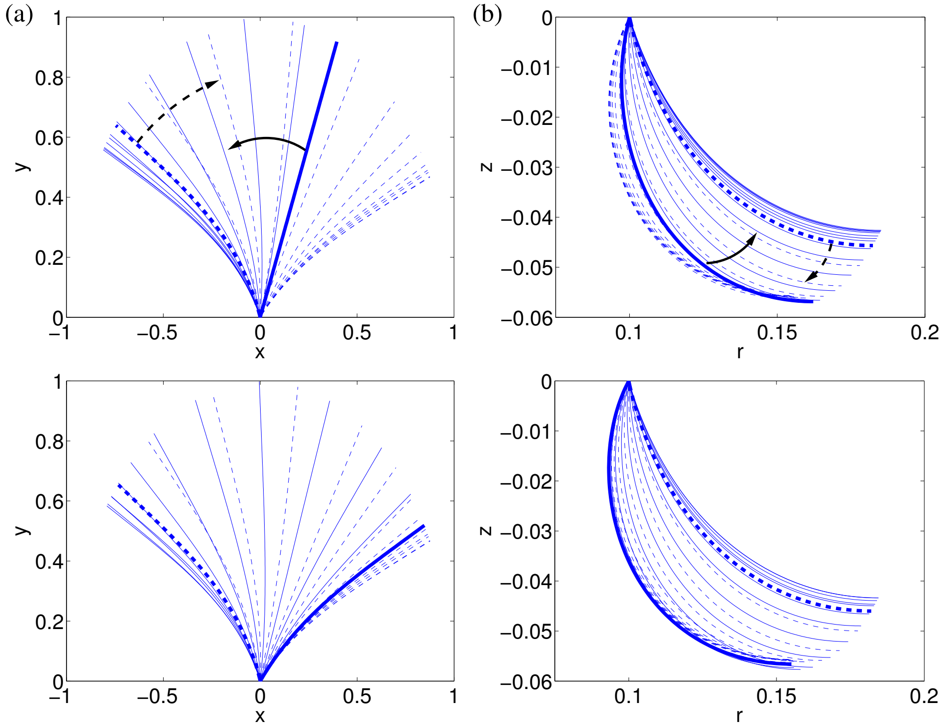

FIGURE 7. Top row: First period of oscillation for an elastic filament with $\eta = 20$ and $\theta_0(t = 0) = 0.37\pi$ in a periodic flow of periodicity 10. Bottom row: Second period of oscillation from $t = 10$ to $t = 20$. Panel (a): Dynamics of the filament. Panel (b): Corresponding deformation of the elastic shell.

at the base reach maximum in the leftward half of the oscillation, while the tangent and normal forces reach maximum magnitude in the rightward half of the period.

3.3. **Effect of base angle for a flexible filament ($\eta = 20$) in an oscillating flow.** Here we study the dynamics of the flexible filament with $\eta = 20$ and three different values for the initial base angle: $\theta_0(t = 0) = 0.5\pi$ (upright position), $\theta_0(t = 0) = 0.37\pi$ (tilted toward the right), and $\theta_0(t = 0) = 0.70\pi$ (tilted toward the left). Figure 10 shows the filament angle at the fixed end (top panel) and at the free end (bottom panel). The solid curves are for the upright position, the dashed curves are for $\theta_0 = 0.70\pi$ and the dash-dotted curves are for $\theta_0 = 0.37\pi$. After the first period we find similar filament angle at free end $\theta_0(s = 1)$ (bottom panel) during the first half of each cycle, while significant difference is found during the second half of each cycle. The corresponding variations of curvature κ, tension, and forces (F^t and F^n) at the fixed filament end ($s = 0$) are shown in figure 10(b) and (c).

Similar to the variation in the filament angle at the free end, the curvature at the fixed end is almost identical during the first one-third period of oscillation. Larger curvature, tension and forces (in magnitude) at the base are observed for the cilium tilted in the flow direction. The axonemal base is where the largest

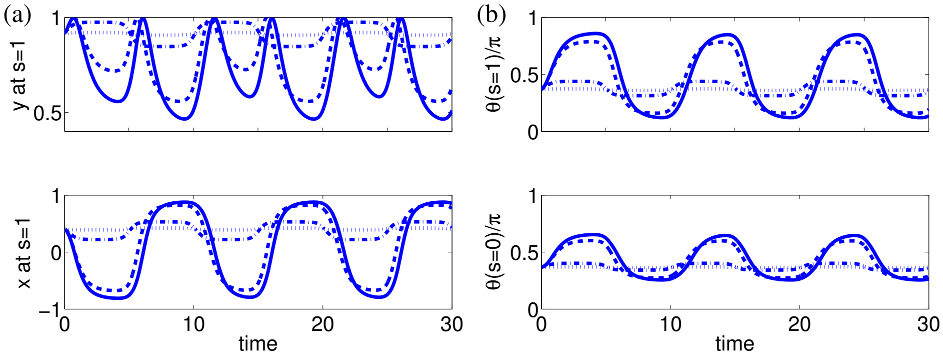

FIGURE 8. Panel (a): Location of the free end ($s = 1$). Panel (b): Angles at the free end (top) and the fixed end (bottom). $\eta = 0.1$ for the dotted lines, $\eta = 1$ for the dash-dotted lines, $\eta = 10$ for the long dashed lines, and $\eta = 20$ for the solid lines.

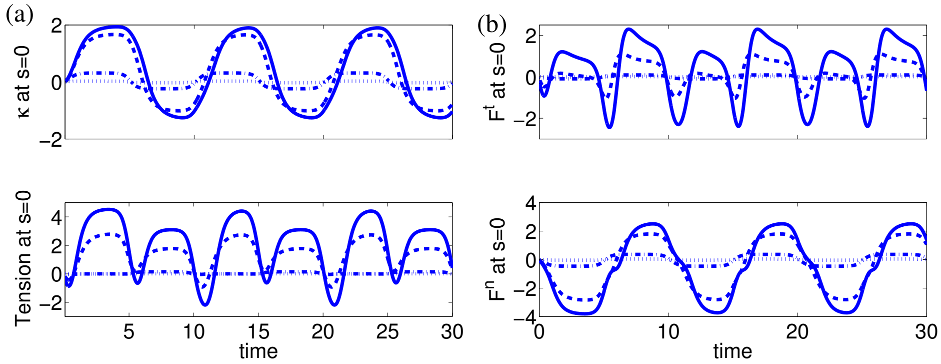

FIGURE 9. Panel (a): Curvature κ (top) and tension (bottom) at the fixed end. Panel (b): Tangential force F^t (top) and normal force F^n (bottom). $\eta = 0.1$ for the dotted lines, $\eta = 1$ for the dash-dotted lines, $\eta = 10$ for the long dashed lines, and $\eta = 20$ for the solid lines.

stress locates when the cilia bend under flow [32, 40]. It has been speculated that such large stress at the base is closely related to the activation of ion channels such as polycystin-2. Therefore our findings show that it is possible to enhance the sensitivity (larger tension and forces at filament base) by slightly tilting the cilium base in the direction of flow.

3.4. **Oscillating versus pulsing flows.** Here we investigate the difference between an oscillating flow and a pulsing flow. For a pulsing flow we use $U = -\frac{1}{2}\left[\tanh(10\sin(\frac{2\pi t}{T}))+1\right](y,0)$: The flow magnitude varies quickly from zero to unity at the beginning, and then transitions smoothly to zero in the second half of the cycle (dashed line in figure 3(c)). Figure 11 shows the comparison of filament free end position (left panels) and angles (right panels) between the two flows for $\eta = 20$, initial filament base angle $\theta_0 = 0.5\pi$, and flow period $T = 10$. After the

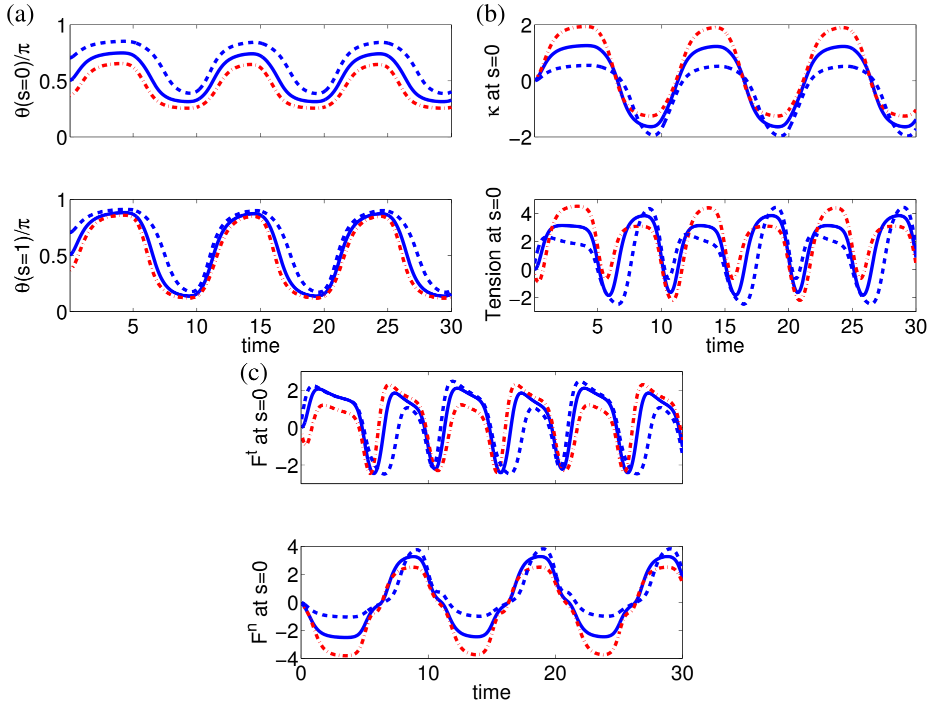

FIGURE 10. $\eta = 20$ with different initial base angles: $\theta_0(t = 0) = 0.5\pi$ for solid lines, $\theta_0(t = 0) = 0.37\pi$ for dash-dotted lines, and $\theta_0(t = 0) = 0.70\pi$ for dashed lines. Panel (a): base angle (top) and angle at the free end (bottom). Panel (b): Curvature κ (top) and tension (bottom) at the fixed end. Panel (c): Tangential force F^t (top) and normal force F^n (bottom).

first transitional period, we find slow relaxation in the second half of each cycle for the pulsaile flow. In addition, the filament stays in the left all through the three periods shown.

Figure 12(a) shows the corresponding variation of filament curvature (top panel) and filament tension (bottom panel) at the fixed end. Figure 12(b) shows the corresponding tangent (top) and normal (bottom) forces at the fixed end. For the pulsatile flow, we observe that the tension stays positive while it changes sign for the oscillating flow. In addition we find that the tangential force F^t reaches a maximum value right after the pulsing flow is turned on, while F^t reaches a minimum when at the beginning of each cycle for the oscillating flow.

4. DISCUSSION AND CONCLUSION

In this work we used the elastic filament-sheet model to simulate the dynamics of a primary cilium under time-periodic fluid flows. Simulation results show that high tension and forces at the cilium base are associated with flexible ciliary axoneme. We also find that a tilt at the base may help the cilium differentiate the flow direction via the forces at the base. In § 3.4 we further compare the dynamics of

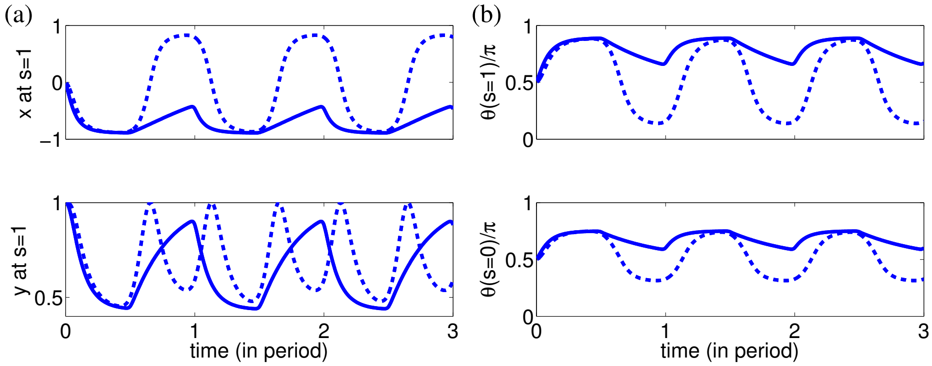

FIGURE 11. Panel (a): Location of the free end ($s = 1$). Panel (b): Angles at the free end (top) and the fixed end (bottom). Flow period $T = 10$. Dashed lines are for oscillating flow and solid lines are for pulsatile flow.

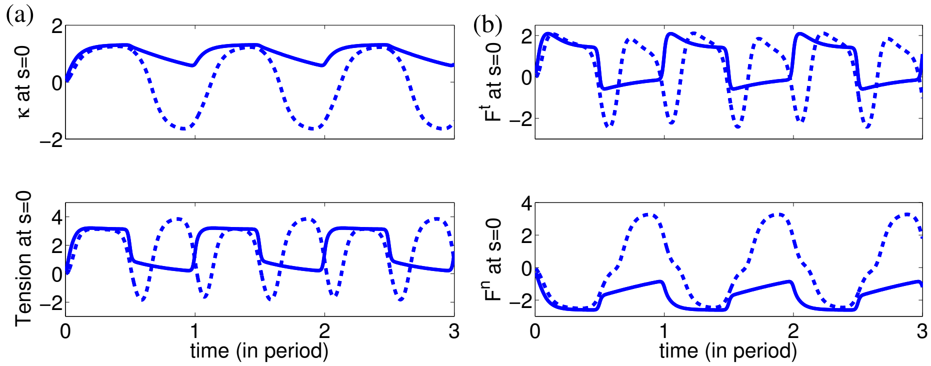

FIGURE 12. Panel (a): Curvature κ (top) and tension (bottom) at the fixed end. Panel (b): Tangential force F^t (top) and normal force F^n (bottom). Flow period $T = 10$. Dashed lines are for oscillating flow and solid lines are for pulsatile flow.

an upright filament with $\eta = 20$ between the oscillating flow and the pulsatile flow of the same period $T = 10$.

In experiments [18, 4] pulsatile flow is more effective than steady or oscillating flow in terms of the fraction of bone cells that respond to the fluid flow stimulation. In addition, it is also found that the pulsatile flow becomes less stimulating as the flow frequency increases. Here we study the effect of frequency of a pulsing flow. Figure 13 shows the curvature, tension and forces at axoneme base plotted against time (in period). Comparing results for all three periods, we find that the frequency does not affect much the magnitude of these variables. Assuming that these high tension and forces along the filament provides a strong likelihood of opening up ion channels near the basal body, we speculate that, over a sufficient duration, large flow-induced cilium bending will stimulate the cellular signaling processes, as suggested by [32]. Therefore the reduction in cellular responses to the mechanical

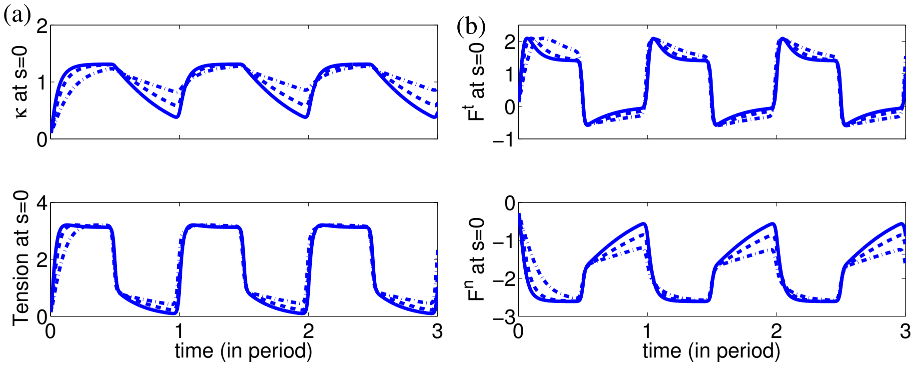

Figure 13. Dynamics at different frequencies with $\eta = 20$, $\theta_0(t = 0) = 0.5\pi$ for the pulsing flow. $T = 15$ for the solid lines, $T = 10$ for the dashed lines and $T = 5$ for the dash-dotted lines. Panel (a): Curvature κ (top) and tension (bottom) at the fixed end. Panel (b): Tangential force F^t (top) and normal force F^n (bottom).

stimulation at high frequencies may be due to (1) the structural change (wear and tear) of ciliary basal body from repetitive bending at high frequencies, or (2) the ion channels do not have time to respond to the stress at high frequencies.

The cellular response to fluid shear stresses is shown to depend on the integrity of microtubular network [16]. Recently it has also been found that the number of microtubules around the primary cilium basal body increases when the cilium is subject to fluid flow stimulation. Accompanied with the increase in microtubules is a morphological change in the microtubule network in response to the stimulation from fluid flow [7]. It will be interesting to compare these results with experimental observations from the oscillatory flow chamber and make quantitative connections with the morphological changes of the cytoskeletal network that is in contact with the basal body.

We are currently working to replace the elastic shell in our filament-sheet model with a cross-linked semi-flexible polymer network to model the cytoskeletal network that is connected with the cilium basal body. The mechanical transduction of such a random, semi-flexible, cross-linked biopolymer network is a very challenging subject because its *in vivo* properties are expected to be highly dependent on the length and time scales on which they are being probed. The static mechanical properties of such networks has been investigated in the linear response regime at zero temperature [13, 14, 36]. Such networks can be constructed by sequential random deposition of monodisperse filaments into a two-dimensional box. Since the position and orientation of filaments are uniformly distributed over the allowed ranges, the networks are isotropic and homogeneous on sufficiently large scales. Each intersection between filaments is a cross link. The elastic moduli can be computed from the discrete Hamiltonian that consists of both the discrete bending energy and compression/extensional energy [2, 15, 24].

ACKNOWLEDGMENTS

YNY acknowledges partial support of NSF from grants CBET-0853673, DMS-0708977, and DMS-0420590 for the computing cluster at NJIT.

References

1. E. J. Arnsdorf, P. Tummala, and C. R. Jacobs, *Wnt signaling and n-cadherin related beta-catenin signaling play a role in mechanically induced osteogenic cell fate*, PLoS One **4** (2009), e5388.
2. M. Bai, A. R. Missel, A. J. Levine, and W. S. Klug, *On the role of the filament length distribution in the mechanics of semiflexible networks*, Acta Biomaterialia **7** (2011), 2109–2118.
3. Robert A. Bloodgood, *From central to rudimentary to primary: The history of an under-appreciated organelle whose time has come. the primary cilium.*, Methods in Cell Biology, Vol. 94: Primary Cilia (Roger D. Sloboda, ed.), Academic Press, San Diego, California, USA, 2009, pp. 3–52.
4. T. L. H. Donahue, T. R. Haut, C. E. Wellowley, H. J. Donahue, and C. R. Jacobs, *Mechanosensitivity of bone cells to oscillating fluid flow induced shear stress may be modulated by chemotransport*, J Biomech **36** (2003), 1363–1371.
5. Matthew E. Downs, An M. Nguyen, Florian A. Herzog, David A. Hoey, and Christopher R. Jacobs, *An experimental and computational analysis of primary cilia deflection under fluid flow*, Computer Methods in Biomechanics and Biomedical Engineering **iFirst** (2012), 1–9.
6. H. W. Ehlen, L. A. Buelens, and A. Vortkamp, *Hedgehog signaling in skeletal development*, Birth Defects Res C Embryo Today **78** (2006), 267–79.
7. L. Espinha and C. Jacobs, Cytoskeleton **preprint** (2013).
8. F. R. Garcia-Gonzalo and J. F. Reiter, *Scoring a backstage pass: Mechanisms of ciliogenesis and ciliary access*, J. Cell Biol. **11** (2012), 697–709.
9. S. Gueron and K. Levit-Gurevich, *A three-dimensional model for ciliary motion based on the internal 9+2 structure*, Proc. R. Soc. Lond. B **268** (2001), 599–607.
10. S. Gueron and N. Liron, *Ciliary motion modeling, and dynamic multicilia interactions*, Biophys. J. **63** (1992), 1045–1058.
11. H. Hagiwara, A. Kano, T. Aoki, and N. Ohwada, *Immunocytochemistry of the striated rootlets associated with solitary cilia in human oviductal secretory cells*, Histochem. Cell Biol. **114** (2000), 205–12.
12. C. J. Haycraft and R. Serra, *Cilia involvement in patterning and maintenance of the skeleton*, Curr. Top Dev Biol **85** (2008), 303–32.
13. D. A. Head, A. J. Levine, and F. C. MacKintosh, *Deformation of cross-linked semiflexible polymer networks*, Phys. Rev. Lett. **91** (2003), 108102.
14. ———, *Distinct regimes of elastic response and deformation modes of cross-linked cytoskeletal and semiflexible polymer networks*, Phys. Rev. E **68** (2003), 061907.
15. ———, *Mechanical response of semiflexible networks to localized perturbations*, Phys. Rev. E **72** (2005), 061914.
16. B. P Hierck, K. Van Der Heiden, F. E. Alkemade, S. Van de Pas, J. V. Van Thienen, B. C. C. Croenendijk, W. H. Bax, A. Van der Laarse, M. C. DeRuiter, A. J. G. Horrevoets, and R. E. Poelmann, *Primary cilia sensitize endothelial cells for fluid shear stress*, Developmental Dynamics **237** (2008), 725–735.
17. Hiroaki Ishikawa and Wallace F. Marshall, *Ciliogenesis: building the cell's antenna*, Nature Review **12** (2011), 222.
18. C. R. Jacobs, C. E. Yellowley, B. R. Davis, Z. Zhou, J. M. Cimbala, and H. J. Donahue, *Differential effect of steady versus oscillating flow on bone cells*, J. Biomech. **31** (1998), 969–976.
19. R. Y. Kwon, D. A. Hoey, and C. R. Jacobs, *Mechanobiology of Primary Cilia*, Cellular and Biomolecular mechanics and mechanobiology (A. Gefen, ed.), Springer, New Jersey, 2011, pp. 99–124.
20. W. Liu, N. S. Murica, Y. Duan, S. Weinbaum, B. K. Yoder, E. Schwiebert, and L. M. Satlin, *Mechanoregulation of intracellular Ca2+ concentration is attenuated in collecting duct of monocilium-impaired orpk mice*, Am. J. Physiol. Renal Physiol. **289** (2005), F978–988.

21. J. R. Marszalek, P. Ruiz-Lozano, E. Roberts, K. R. Chien, and L. S. Goldstein, *Situs inversus and embryonic ciliary morphogenesis defects in mouse mutants lacking the kif3a subunit of kinesin-ii*, Proc. Natl Acad Sci USA **114** (1999), 205–12.
22. A. I. Masyuk, T. V. Masyuk, P. L. Splinter, B. Q. Huang, A. J. Stroope, and N. F. LaRusso, *Cholangiocyte cilia detect changes in luminal fluid flow and transmit them into intracellular Ca2+ and cAMP signaling*, Gastroenterology **131** (2006), 911–20.
23. S. M. Nauli, F. J. Alenghat, Y. Luo, E. Williams, P. Vassilev, X. Li, A. E. Elia, W. Lu, E. M. Brown, S. J. Quinn, D. E. Ingber, and J. Zhou, *Polycistins 1 and 2 mediate mechanosensation in the priimary cilium of kidney cells*, Nat Genet **33** (2003), 129–37.
24. R. C. Picu, *Mechanics of random fiber networks - a review*, Soft Matter **7** (2012), 6768–6785.
25. Aleksander S. Popel, Bahman Anvari, William E. Brownell, and Alexander A. Spector, *Modeling the mechanics of tethers pulled from the cochlear outer hair cell membrane*, J. Biomechanical Eng. **130** (2008), 031007.
26. C. Pozrikidis, *Shear flow over cylindrical rods attached to a substrate*, Fluids and Structures **26** (2010), 393–405.
27. ———, *Shear flow past slender elastic rods attached to a plane*, International Journal of Solids and Structures **48** (2011), 137–143.
28. H. A. Praetorius and K. R. Spring, *Bending the mdck cell primary cilium increases intracellular calcium*, J. Membr. Biol. **184** (2001), 71–9.
29. ———, *Removal of the mdck cell primary cilium abolishes flow sensing*, J. Membr. Biol. **191** (2003), 69–76.
30. Andrew Resnick and Ulrich Hopfer, *Mechanical stimulation of primary cilia*, Frontiers in Bioscience **13** (2008), 1665–1680.
31. Rajat Rohatgi and William J. Snell, *The ciliary membrane*, Current Opinion in Cell Biology **22** (2010), 541–546.
32. Susanna Rydholm, Gordon Zwartz, Jacob M. Kowalewski, Padideh Kamali-Zare, Thomas Frisk, and Hjalmar Brismar, *Mechanical properties of primary cilia regulate the response to fluid flow*, Am. J. Physiol. Renal. Physiol. **298** (2010), F1096–F1102.
33. Peter Satir, Lotte B. Pedersen, and Soren T. Christensen, *The primary cilium at a glance*, Cell Science at a Glance **123** (2010), 499–503.
34. Kristopher R. Schumacher, Aleksander S. Popel, Bahman Anvari, William E. Brownell, and Alexander A. Spector, *Computational analysis of the tether-pulling experiment to probe plasma membrane-cytoskeleton interaction in cells*, Phys. Rev. E **80** (2009), 041905.
35. Eric A. Schwartz, Michelle L. Leonard, Rena Bizios, and Samuel S. Bowser, *Analysis and modeling of the primary cilium bending response to fluid shear*, Am. J. Physiol. **272** (1997), F132–F138.
36. A. Shahsavari and R. C. Picu, *Model selection for athermal cross-linked fiber networks*, Phys. Rev. E **86** (2012), 011923.
37. Anna-Karin Tornberg and Michael J. Shelley, *Simulating the dynamics and interactions of flexible fibers in Stokes flows*, J. Comp. Phys. **196** (2004), 8–40.
38. Y.-N. Young, *Hydrodynamic interactions between two semiflexible inextensible filaments in Stokes flow*, Phys. Rev. E **79** (2009), 046317.
39. ———, *Dynamics of a compound vesicle in shear flow*, Phys. Rev. E **82** (2010), 016309.
40. Y.-N. Young, M. Downs, and C. R. Jacobs, *Dynamics of the primary cilium in shear flow*, Biophys. J. **103** (2012), 629–639.

DEPARTMENT OF MATHEMATICAL SCIENCES, AND CENTER FOR APPLIED MATHEMATICS AND STATISTICS, NEW JERSEY INSTITUTE OF TECHNOLOGY, NEWARK, NEW JERSEY 07102 USA,
E-mail address: `yyoung@njit.edu`